JOURNAL OF
SYNCHROTRON
RADIATION

ISSN 1600-5775

Calculating absorption dose when X-ray irradiation modifies material quantity and chemistry

Viatcheslav Berejnov,[a]* Boris Rubinstein,[b] Lis G. A. Melo[c]‡ and Adam P. Hitchcock[c]

[a]Analytical Laboratory, FTXT Energy Technology Co. Ltd, 2199 Chaoyang Street, Baoding, Hebei 071000, People's Republic of China, [b]Stowers Institute for Medical Research, 1000 East 50th Street, Kansas City, MO 64110, USA, and [c]Department of Chemistry and Chemical Biology, McMaster University, Hamilton, ON, Canada L8S 4M1. *Correspondence e-mail: berejnov@gmail.com

Received 5 December 2020
Accepted 11 February 2021

Edited by S. M. Heald, Argonne National Laboratory, USA

‡ Current address: Department of Chemistry, Simon Fraser University, Burnaby, Canada.

Keywords: soft X-rays; fluoropolymers; radiation dose; STXM; linear absorption coefficient; elemental molecular unit.

Supporting information: this article has supporting information at journals.iucr.org/s

X-ray absorption is a sensitive and versatile tool for chemical speciation. However, when high doses are used, the absorbed energy can change the composition, amount and structure of the native material, thereby changing the aspects of the absorption process on which speciation is based. How can one calculate the dose when X-ray irradiation affects the chemistry and changes the amount of the material? This paper presents an assumption-free approach which can retrieve from the experimental data all dose-sensitive parameters – absorption coefficients, composition (elemental molecular units), material densities – which can then be used to calculate accurate doses as a function of irradiation. This approach is illustrated using X-ray damage to a solid film of a perfluorosulfonic acid fluoropolymer in a scanning transmission soft X-ray microscope. This new approach is compared against existing dose models which calculate the dose by making simplifying assumptions regarding the material quantity, density and chemistry. While the detailed measurements used in this approach go beyond typical methods to experimental analytical X-ray absorption, they provide a more accurate quantitation of radiation dose, and help to understand mechanisms of radiation damage.

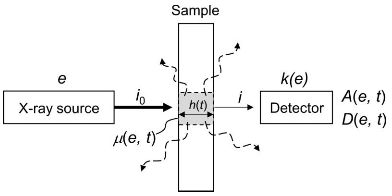

1. Introduction

Soft X-ray ionizing radiation is increasingly used for material characterization of fluorinated or organic compounds and their polymers (Hitchcock *et al.*, 2016; Ade & Hitchcock, 2008). Achieving better quality spectroscopy and imaging requires a higher signal-to-noise ratio for the ionizing radiation reaching the detector, which implies higher intensity of incident soft X-rays (Starodub *et al.*, 2008). However, high X-ray intensity often leads to high absorbed dose, which can damage the sample material, modifying its initial physical-chemical state by breaking existing and creating new chemical bonds (Wang, Morin *et al.*, 2009; Egerton *et al.*, 2015; Yang & Wang, 2017). The extent of radiation-induced damage is related to the amount of energy absorbed per unit mass of the material, otherwise known as the radiation dose, D, which is expressed in units of Grays (1 Gy = 1 J/1 kg). The relationship between the absorbed dose and its ensuing damage defines the ability of a given material to withstand the applied radiation. From a practical perspective, radiation damage modifies the spectral signal making its interpretation less clear, thereby diminishing the benefits of high-intensity incident X-rays for analytical studies. Therefore, proper monitoring of the dose and quantitation of both the dose and the extent of damage is becoming increasingly important for optimization of analytical characterization methods employing soft X-rays as a probe (Wu, Melo *et al.*, 2018; Wu, Zhu *et al.*, 2018).

For methods based on X-ray transmission, the common approach to estimating the dose is to record the evolution of the absorption spectrum, measured as a photon energy (e) and time (t) dependent optical density, $A(e, t)$. Once the optical density function $A(e, t)$ is known for a particular time interval $(0, t)$, the corresponding dose can be calculated, taking into account a particular model of the evolution of the chemistry and mass $M(t)$ of the material during the measurements. Currently, there are three models for dose calculation. Their difference is linked to the different types of response of materials to the applied X-ray irradiation. The optical density function is usually referred to as the near-edge X-ray absorption fine-structure (NEXAFS) spectrum (Stöhr, 1992). The NEXAFS spectra at the absorption edges of each of the atoms constituting the material are specific to that material (see Fig. 1), making NEXAFS a convenient tool for material identification and for quantifying the effect of radiation damage (Coffey *et al.*, 2002; Wang, Morin *et al.*, 2009).

The first model, the simplest one, is when neither A nor M depend on time during the X-ray exposure, Fig. 1(*a*). This model is widespread but it can only be applied for damage-resistive materials or when the irradiation time is shorter than the time for significant radiation-induced change. The second model is when the optical density function depends on time $A(e, t)$ for some photon energy interval (e_1, e_2), while the material mass M is not, Fig. 1(*b*). This model can be used for certain cases of photochemical reactions triggered by X-ray irradiation where the products do not leave the irradiated volume (Leontowich *et al.*, 2012; Wang, Morin *et al.*, 2009). In applying this model, it is assumed that the absorbed X-rays reconfigure the chemical bonds in the material while the number of atoms in the irradiated zone stays constant [*i.e.* the spectral curves in Figs. 1(*a*) and 1(*b*) have the same value of the pre-edge, $A_{\rm pr}$, and post-edge absorption $A_{\rm pst}$, indicating conservation of the mass]. The third model involves cases where both $A(e, t)$ and $M(t)$ are time (*i.e.* dose) dependent, Fig. 1(*c*). In such situations it is necessary to consider the chemical changes and the mass loss (removal of selected atoms from the irradiated volume) as a function of applied dose (Berejnov *et al.*, 2018). The appropriate model to use depends on the types of changes of the optical density $A(e, t)$ with respect to the X-ray photon energy e and irradiation time t, *i.e.* how the NEXAFS spectrum over a selected energy interval changes with respect to irradiation time (Fig. 1).

Although the third model seems to be most general (Berejnov *et al.*, 2018), it also has a significant assumption (inherited from the second model) – that the linear absorption coefficient of the material, μ, is independent of the dose. This assumption limits applications of the third model to cases where material removal due to radiation could be significant but chemical changes of the irradiated material (described by μ, indicating elemental composition) are insignificant, *i.e.* radiation removes material in the form of material units, *i.e.* molecules or polymer repeat units, conserving the initial elemental composition. A similar concern relates to the assumption that the density of the material in the irradiated area does not change with dose.

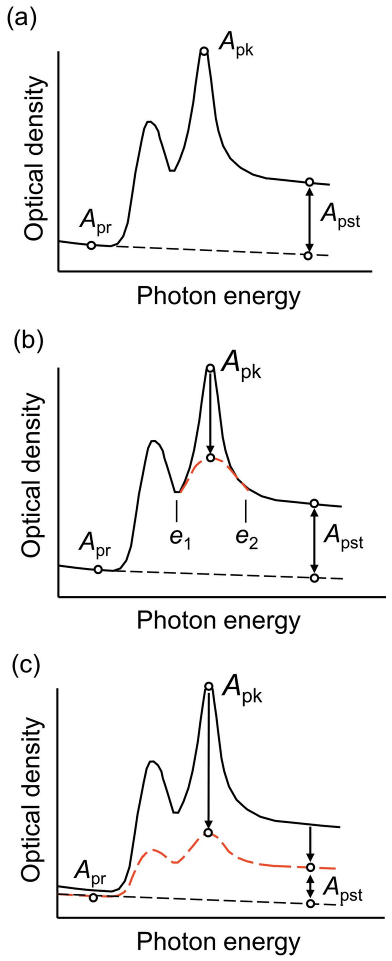

Figure 1
Three models of the absorption spectral change for different damage processes upon X-ray irradiation. (*a*) The applied X-ray irradiation does not change the near-edge X-ray absorption fine-structure (NEXAFS) spectrum: the pre-edge $A_{\rm pr}$, the post-edge $A_{\rm pst}$ and the peak $A_{\rm pk}$ optical densities do not change with the dose applied. (*b*) The peak $A_{\rm pk}$, corresponding to a particular molecular bond or functional group, decays due to the irradiation applied, while $A_{\rm pr}$ and $A_{\rm pst}$ are unchanged. (*c*) Irradiation affects the whole NEXAFS spectrum: the $A_{\rm pr}$ value decays due to changed contributions from different elements, the peak value $A_{\rm pk}$ decays due to X-ray induced chemical reactions and the post-edge $A_{\rm pst}$ decays due to removal of atoms from the X-ray probe volume. The black curve is the initial spectrum, the red dashed curve is the result of irradiation, the black dashed curve is an extrapolation of the pre-edge signal, while the change in $A_{\rm pst}$ relative to the extrapolated $A_{\rm pr}$ value indicates the amount of that element.

Here we outline a new approach which treats cases where the linear absorption coefficient μ changes as a function of the radiation damage. We demonstrate how to include dose-dependent variations of the composition and material density and show that the new model is able to address significant changes in material amount and the chemical composition. The theoretical approach and how it can be applied practically to interpret experiment data are presented. The procedure is illustrated and evaluated using experimental, dose-dependent spectra of perfluorosulfonic acid (PFSA), a fluoropolymer used as an ionic conductor in fuel cells and electrolysers.

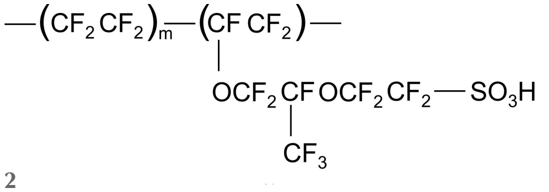

Figure 2
Structure of the repeat unit of the perfluorosulfonic acid (PFSA) used in this work, Nafion$^{\rm TM}$ D521, with the equivalent weight (EW) = 1100 (m = 6.6) (taken from NafRef: https://www.sigmaaldrich.com/technical-documents/articles/materials-science/perfluorosulfonic-acid-membranes.html).

PFSA, see Fig. 2, has S 2p, C 1s, O 1s and F 1s spectra which are sensitive to X-ray radiation to different extents. The presented method derives the elemental linear absorption coefficients $\mu(e, t)$ for the radiation-damaged samples as a function of the applied radiation and recovers the elemental composition at different radiation doses. Describing the radiation damage through changes of the linear absorption coefficients $\mu(e, t)$ allows accurate calculation of the dose imparted to the damaged sample when the chemical composition, thickness and density of the sample change with dose. The new model is compared with the predictions of the three previous models (Berejnov *et al.*, 2018), applied to the same experimental data set. This approach goes beyond typical methods to experimental analytical X-ray absorption. One would not be expected to do this type of detailed study in all cases. However, the approach provides a more accurate evaluation of radiation dose than prior methods, and should be considered when more accurate dose-damage descriptions are needed, such as in cases of multi-step mechanisms of radiation damage.

2. Theory and methods

2.1. Calculating dose D when mass and chemistry change

When a homogeneous sample is exposed for the time interval (0, t = θ) to soft X-ray photons of energy e, the absorbed dose $D(e, t)$ can be calculated as a time integral of the ratio of $\dot{E}(e,t)$, the rate of absorbed energy (*i.e.* the number of absorbed photons of energy e per unit of time), to $M(t)$, the mass of the sample exposed (Berejnov *et al.*, 2018),

$$D(e,t=\theta)=\int\limits_0^\theta \frac{\dot{E}(e,t)}{M(t)}\,{\rm d}t, \qquad (1)$$

where t and θ are the integrand time variable and an elapsed time, respectively.[1] We assume that the absorption of the soft X-ray photons follows the Beer–Lambert law, $i(e,t)$ = $i_0(e)\exp(-A(e,t))$, where i_0 and i are time-independent incident and time-dependent transmitted X-ray intensities at energy e, and A is the optical density, also symbolized as OD. The irradiated sample mass is given by $M(t) = \rho(t)\,h(t)\,s$, where $\rho(t)$ is the sample density, s is the cross-sectional area of the photon beam and $h(t)$ is the path length of the photon beam in the material, which is the same as the 'material thickness', Fig. 3. We assume that the material is sufficiently thin that some X-rays pass through the material and that the Beer–Lambert law holds.[2] The dose in equation (1) can then be expressed as

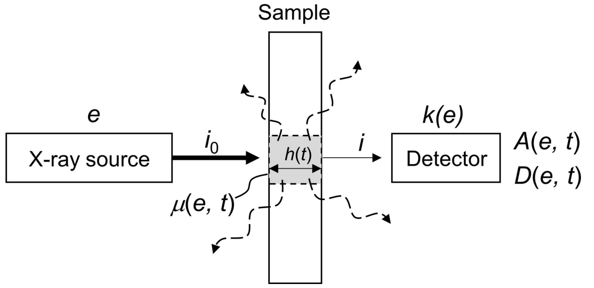

Figure 3
Simplified sketch of the experiment, identifying key parameters. Dashed arrows indicate mass loss from the irradiated sample volume (gray box). The irradiated part of the sample has an absorption coefficient $\mu(e, t)$, which is different from the non-irradiated part (white boxes).

$$D(e,t=\theta)=\frac{e i_0(e)}{k(e)\,s}\int\limits_0^\theta \frac{\mu(e,t)}{\rho(t)}\,\frac{1-\exp(-A(e,t))}{A(e,t)}\,{\rm d}t, \qquad (2)$$

where $h(t)$ has been substituted by the ratio of the optical density and the linear absorption coefficient $h(t)$ = $A(e,t)/\mu(e,t)$. The variable $k(e)$ is the X-ray energy-dependent detector efficiency, Fig. 3.

In general, when radiation damage occurs: (i) the linear absorption coefficient $\mu(e, t)$ and the optical density $A(e, t)$[3] become functions of time for a given photon energy; and (ii) the material density $\rho(t)$ is a function of time. The parameters μ and ρ are properties of the material, while A and h are properties of the specific sample and conditions of measurement. Note that μ for h = 1 nm is also known as the OD1 coefficient (Hitchcock *et al.*, 2012). This approach disregards where exactly along the beam path in the sample the radiation damage and, thus, variations of μ and ρ occur. Therefore, μ and ρ describe *effective* properties of the material along the optical path of the beam in the sample with an *effective* thickness h, Fig. 3. In the *Discussion* we suggest a method for obtaining values for μ and ρ that vary with distance along the path, h.

If the linear absorption coefficient and material density are *time independent*, and the material density is known, then it is possible to compute the integral in equation (2) analytically, or approximate it with a good accuracy for any function of optical density $A(e, t)$ (Berejnov *et al.*, 2018). However, when the linear absorption coefficient and/or the material density *depends on time*, the functions $\mu(e, t)$, $\rho(t)$ and $A(e, t)$ must be known in order to compute the integral (2).

---

[1] Table S-1 of the supporting information lists all symbols used in this article, with definitions and units.

[2] In the instrument used for the experimental part of this work, absorption saturation of sharp peaks can start to occur for OD values as low as 2.5.

[3] Although A and μ are generally considered synonyms, in this article we reserve μ to refer to the elemental response while we use A to refer to the complete NEXAFS spectrum.

It is possible to compute the dose integral, equation (2), numerically by partitioning the interval of integration $(0, t)$ and obtaining values of μ, ρ and A for each particular time interval from the experiment. This approach requires measurements of μ, ρ and A at a variety of discrete photon energies and irradiation times. During such an experiment a homogeneous sample with a uniform initial thickness undergoes a series of exposures $(t_1, t_2, \ldots, t_i)$, each of which is applied to different, not previously exposed, areas – a pad (Wang, Morin *et al.*, 2009). In this case, after all irradiations are done, the values of $\mu(e, t)$ and $A(e, t)$ can be obtained by analysis of the spectroscopic data (measured under negligible dose conditions) and attributed to a particular ith pad $(1, 2, \ldots)$ of a multi-pad exposure, Fig. 4. Combining μ and independent measurements of the geometrical thickness of each pad, made by atomic force microscopy (AFM) for example, $\rho(t)$ can be calculated. Then, the dose integral $D(e, t_i)$, equation (2), can be approximated by partitioning the interval of integration $(0, t_i)$ according to the exposure time intervals $((0, t_1), (t_1, t_2), \ldots, (t_{i-1}, t_i))$ and a corresponding series of: linear absorption coefficients $(\mu_1 = \mu(e, t_1)$, $\mu_2 = \mu(e, t_2), \ldots, \mu_i = \mu(e, t_i))$, absorption optical densities $(A_1 = A(e, t_1)$, $A_2 = A(e, t_2), \ldots, A_i = A(e, t_i))$ and material densities $(\rho_1 = \rho(t_1)$, $\rho_2 = \rho(t_2), \ldots, \rho_i = \rho(t_i))$ for each pad.

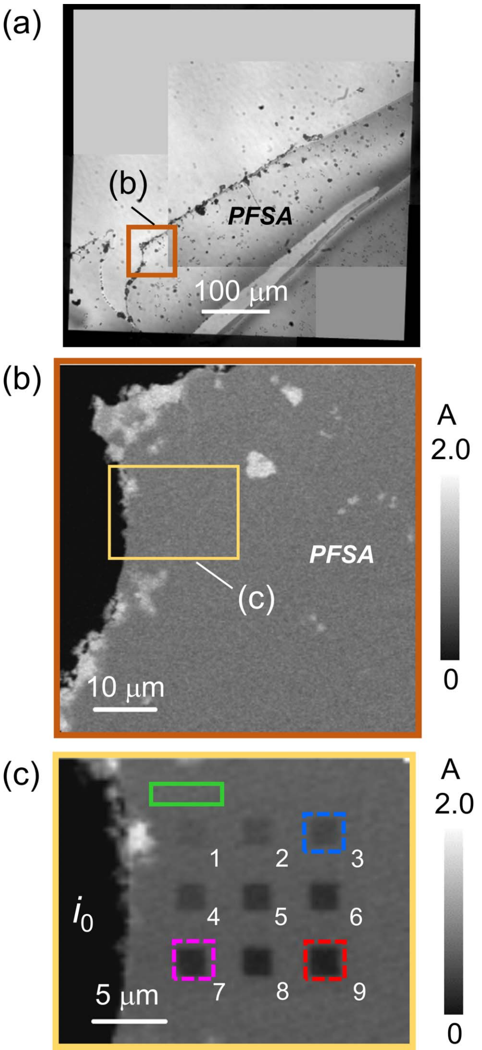

Figure 4
(*a*) Optical microscopy image in reflectance mode of a PFSA spin-coated film deposited on a silicon nitride (SiN_x) window for STXM damage experiments. Panels (*b*) and (*c*) are STXM optical density (OD) images: panel (*b*) was measured before the 9-pad radiation damage experiment at 292.4 eV; panel (*c*) is the rectangular area in (*b*), measured at 690 eV after the 9-pad pattern was burned at 320 eV. The area labeled i_0 indicates the region that can be used to measure the incident X-ray intensity. Numbers in (*c*) denote the pad index, the green area is non-damaged PFSA(1100), while the blue, magenta and red boxes indicate pads 3, 7 and 9.

When the values of μ_i, ρ_i and A_i are known for each pad (with index i), the expression (2) must be adapted for calculating the dose via a recursion method which allows calculation of the dose for each pad, *i.e.* for each exposure time interval.

The first pad receives the dose $D(e, (0, t_1))$ from the radiation exposure $(0, t_1)$ which changes the nature of the material in the pad. Its linear absorption coefficient $\mu_1 = \mu(e, t_1)$ and its material density $\rho_1 = \rho(t_1)$ are such that pad 1 has the optical density $A_1 = A(e, t_1)$. The dose $D_1 = D(e, (0, t_1))$ is then calculated as follows,

$$\begin{aligned} D_1 &= D(e, (0, t_1)) \\ &= \frac{e i_0(e)}{k(e)\, s\rho(t_1)}\, \mu(e, t_1)\, \frac{1 - \exp(-A(e, t_1))}{A(e, t_1)}\, (t_1 - 0) \\ &= L_1 \mu_1 T_{0,1}. \end{aligned} \tag{3}$$

Note, functions L_i and $T_{0,1}$ are defined below. Experimentally, the exposure time for pad 2 is longer than for pad 1 and is the sum of intervals $(0, t_1) + (t_1, t_2)$. Therefore, for the time interval $(0, t_1)$, pad 2 receives the same dose as pad 1 and experiences the same damage as pad 1, characterized by μ_1, ρ_1 and A_1. For the time interval (t_1, t_2), pad 2 receives an additional dose and thus experiences additional damage characterized by μ_2, ρ_2 and A_2. The dose D_2 received by pad 2 is calculated as a sum of doses received for the two consecutive time intervals,

$$D_2 = D(e, (0, t_2)) = D(e, (0, t_1)) + D(e, (t_1, t_2)), \tag{4}$$

where $D(e, (t_1, t_2))$ is calculated in a way similar to equation (3), namely

$$D(e, (t_1, t_2)) = L_2 \mu_2 \frac{1 - \exp(-A(e, t_2))}{A(e, t_2)} (t_2 - t_1). \tag{5}$$

Finally, the total dose for pad 2, D_2, is

$$D_2 = D_1 + L_2 \mu_2 T_{1,2}. \tag{6}$$

The dose D_3 received by pad 3 is calculated by using a recursion procedure analogous to equations (4) and (6),

$$D_3 = D_2 + L_3 \mu_3 T_{2,3}, \tag{7}$$

where $D(e, (t_2, t_3))$ is calculated similar to $D(e, (t_1, t_2))$ using equation (5) but with changed integration limits. This procedure can be continued to pad 4 to evaluate $D_4(e, t_4)$, and so on to the last pad. The expression for the function $L_i(e, t)$ is

$$L_i = L(e, t_i) = \frac{e i_0(e)}{k(e)\, s\rho(t_i)}. \tag{8}$$

This function denotes the linear dose rate, a dose rate per length of the sample thickness. Note, the product of $L(e, t)$ and μ gives the usual dose rate (Berejnov *et al.*, 2018). The expression for the function $T_{i-1,i}(e, t)$ is

$$T_{i-1,i} = T(e, \Delta t) = \frac{1 - \exp(-A(e, t_i))}{A(e, t_i)} \, (t_i - t_{i-1}), \qquad (9)$$

which is the effective time integral introduced by Berejnov *et al.* (2018).

In general, the dose received by the ith pad is calculated based on the dose received by the $(i - 1)$th pad using the following recursion,

$$D_i = D_{i-1} + D(e, (t_{i-1}, t_i)), \qquad (10)$$

where the additional dose $D(e, (t_{i-1}, t_i))$ in the time interval (t_{i-1}, t_i) is given by

$$D(e, (t_{i-1}, t_i)) = L_i \mu_i T_{i-1,\,i}, \qquad (11a)$$

where the integral $T_{i-1,i}$ can be calculated analytically (Berejnov *et al.*, 2018) or numerically. Applying a rectangular (simplest) type of partitioning (Atkinson, 1989) for the time argument in the integral of equation (11*a*), the additional dose for each pad has the following numerical form,

$$D(e, (t_{i-1}, t_i)) = L_i \mu_i \, \frac{1 - \exp(-A(e, t_i))}{A(e, t_i)} \, (t_i - t_{i-1}). \qquad (11b)$$

The recursion procedure indicated in equations (10) and (11*b*) is a numerical approach for calculating the dose if the values of $\mu_i = \mu(e, t_i)$, $\rho_i = \rho(e, t_i)$ and the mean value $A_i = A(e, t_i)$ for the particular ith pad are known. Those values must be obtained experimentally.

2.2. Obtaining $\mu(e, t)$ and $A(e, t)$

Irradiation under different conditions can cause different extents and types of material damage. In vacuum, material damage can be described in terms of two parts: (i) structural, *i.e.* changes of molecular bonding between the atoms composing the material; and (ii) composition, *i.e.* changes in the number of each type of atom in the exposed volume, Fig. 3. Experimentally, the first type of damage causes changes to the near-edge component of the NEXAFS spectra at different edges relative to those of the non-exposed material, Fig. 1(*b*). The second type of damage changes the *pre-* and *post*-edge signal, which is determined by the distribution of elements, not the nature of the bonding, Fig. 1(*c*). The functions μ and A for each time interval of irradiation can be determined from experiment and an appropriate analysis of the data, as presented below.

2.2.1. Pattern generation. First, the pattern of nine pads is generated at a specific photon energy e_D in an area of uniform thickness and free of ad-particles, as measured by scanning transmission soft X-ray microscopy (STXM). Fig. 4(*a*) is an optical image of the spun-coated PFSA film (Nafion$^{\rm TM}$ type of ionomer). Fig. 4(*b*) is a STXM OD image recorded at 292.4 eV before pattern generation in order to verify a clean, uniform thickness area (a rectangular box). Fig. 4(*c*) is a STXM OD image at 690 eV, which was used to visualize the 9-pad pattern. While we have found the 9-pad arrangement to be efficient, flexible and with sufficient sampling for quantitative analysis of X-ray damage, other exposure arrangements could also be used (linear arrangement, circles instead of square pads, more than 9 pads, *etc.*). Each pad is generated in the same way (beam properties, inter-pad spacing of the 10 × 10 pixels used to create each pad, *etc.*) except for a different exposure time t_i. Here, we assume that the extent of damage is only dependent on the absorbed dose and not the photon energy of the exposure. This has been demonstrated experimentally in several cases (Wang, Morin *et al.*, 2009; Wang, Botton *et al.*, 2009; Leontowich *et al.*, 2016). In this paper, the samples were exposed at energies in a regime of continuum absorption, away from intense, sharp resonances, so that the results are not sensitive to small changes in photon energy.

2.2.2. Optical density imaging. Second, OD images are acquired for the whole 9-pad pattern including non-exposed areas of the sample at the photon energy with the greatest sensitivity to the changes caused by the radiation damage, e_A (often the energy of highest absorption) and at the damage photon energy e_D, Fig. 4(*c*). The image at e_A allows to visualize the 9-pad damage pattern and navigate to a particular pad. The image at the damage energy e_D provides values of the function $A(e_D, t_i)$ for equation (11). It is useful to record the OD image at e_D before pattern generation, Fig. 4(*b*), as it can be used to normalize post-exposure images to remove the effect of any initial sample thickness variation in the region of the 9-pad pattern.

2.2.3. Spectroscopy. Third, an image sequence, also called a stack (Jacobsen *et al.*, 2000), over the *absorption edge of each element* in the material is recorded in order to obtain absorption spectra of each pad, and thus enable determination of the spectrum of the *elemental* linear absorption coefficient μ for each pad. The NEXAFS spectra are obtained for n absorption edges corresponding to the n elements contributing most to the pad material absorption, Fig. 5. Those NEXAFS spectra are the optical density functions $A_n(e, t_i)$ acquired for each of the ith pads for the series of consecutive discreet photon energies in the interval of the photon energy Δe selected around a particular edge. The selection of the absorption edges, their number n, and the intervals of photon energy, Δe_n, of each edge depends on the type of atoms constituting the particular material, *i.e.* on the chemistry of the particular material. The set of NEXAFS spectra are combined into a piecewise optical density function $A_i(e, t) = (A_1(\Delta e_1, t_i), A_2(\Delta e_2, t_i), \ldots, A_n(\Delta e_n, t_i))$ with photon energy e as a variable and t_i as a parameter of the ith pad. Fig. 5 presents an example (with a constant density) of the piecewise optical density function $(A_1(\Delta e_1, t_i), A_2(\Delta e_2, t_i))$ consisting of $n = 2$ absorption edges. The piecewise optical density function provides the raw data for obtaining a linear absorption coefficient of the material in the ith pad, Fig. 5. At each edge one defines a pre-edge (Δe_-) and a post-edge (Δe_+) photon energy interval which are used to obtain the linear absorption coefficient μ for the elemental composition of the i-th pad. The absorption at these intervals, Δe_- and Δe_+, away from the bonding-sensitive near-edge structure, depends only on elemental composition

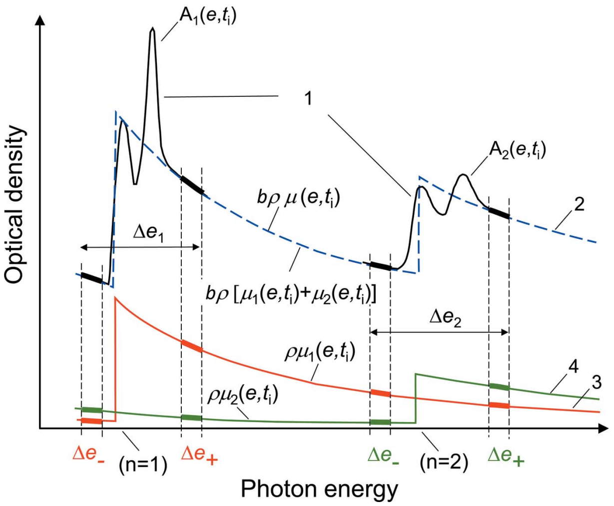

Figure 5
Simplified schematic of fitting two edges of a NEXAFS spectra 1 (black, solid) corresponding to a material having two elemental components: edge 1 – $A_1(\Delta e_1, t)$; and edge 2 – $A_2(\Delta e_2, t)$. Two elemental spectra – 3 (red) and 4 (green) – corresponding to the elemental linear absorption coefficients μ_1 and μ_2, are used for fitting. The resulting fit is curve 2 (blue dashed). Fitting is applied for the photon energy intervals of the pre-edge Δe_- and post-edge Δe_+ of the both edges (thick parts of curves). b is a fitting coefficient related to the material thickness.

(Henke *et al.*, 1993; Hitchcock, 2012) providing the elemental components μ_1 and μ_2 of the material linear absorption coefficient μ. We note in this article μ represents the *elemental part* of the overall linear absorption coefficient.

2.2.4. Calculating $\mu(e, t_i)$ from the experimental data. The linear absorption coefficient μ (cm^{-1}) of the material is proportional to the mass absorption coefficient μ_m (cm^2 g^{-1}), $\mu = \rho\mu_m$, where ρ is the density (g cm^{-3}) of the material. If the material is composed of only one type of atom, then the mass absorption coefficient is the ratio of the photon-energy-dependent cross-section of the atom, σ (10^{-24} cm^2 atom^{-1}) to an average mass of the atom m_a (g), $\mu_m = \sigma/m_a$. The atomic cross-section depends on the photon energy (Henke *et al.*, 1993). If the material is composed of repetitive molecular units or unit cells, then both the cross-section and the mass of the repeat unit should be used for this analysis.

For the molecular unit, it is convenient to introduce three arrays. First, the *elemental atomic array* of the unit, $\mathbf{a} = (a_1, a_2, \ldots, a_n)$, denotes an array of n-types of different atoms, each of those present $a_1, a_2, \ldots, a_n$ times in the molecular unit. Second, the *elemental cross-section array* of the unit, $\boldsymbol{\sigma} = (\sigma_1, \sigma_2, \ldots, \sigma_n)$ denotes an array of atomic cross-sections of n different types of atoms composing the molecular unit of the given material. Third, $\mathbf{M}_r = (M_{r,1}, M_{r,2}, M_{r,n})$ is the *array of molar masses* (g mol^{-1}) of n different atoms in the molecular unit. Combining those arrays as a scalar product gives the following expression (see Section SI1.1 of the supporting information) for the mass absorption coefficient for the material *unit*,

$$\mu_m(unit) = \frac{\sigma(unit)}{m_a(unit)} = N_a \frac{(\boldsymbol{\sigma}\cdot\mathbf{a})}{(\mathbf{M}_r\cdot\mathbf{a})}, \qquad (12)$$

where N_a is Avogadro's constant (mol^{-1}). Equation (12) expresses the functional dependency of the mass absorption coefficient on the elemental array $\mathbf{a}$, $\mu_m(e, \mathbf{a})$. Therefore, if the radiation damage is of type (ii), *i.e.* the distribution of atoms in the irradiated zone changes with increasing dose (for example, fluorine mass loss in the case of PFSA), then the elemental array would be a function of the exposure time, $\mathbf{a}(t)$. Thus, the mass absorption coefficient would also be a function of the time $\mu_m(e, \mathbf{a}(t))$.

Equation (12) reduces the problem of calculating μ to the problem of obtaining the elemental array $\mathbf{a}$. If the elemental array $\mathbf{a}$ is known, either from theory or experiment, then equation (12) allows to calculate μ_m, and then μ (if the material density is known). However, equation (12) is not suitable for obtaining $\mathbf{a}$ (Section SI1.1) – because $\mathbf{a}$ contributes both the numerator and denominator of equation (12). In order to develop a convenient method of obtaining the direct components of the array $\mathbf{a}$, equation (12) must be rearranged to a form in which the linear absorption coefficient μ is related to material density ρ, where ρ is expressed in terms of the molar volume of the material unit, ν (cm^3 mol^{-1}), $\rho = (\mathbf{M}_r \cdot \mathbf{a})/\nu$. Here, $\nu = sh/N$, where s is the beam cross-section, h is the material thickness along the beam (the beam is orthogonal to the sample) and N is the number of moles of the material in the volume, sh. After canceling the scalar products the expression for the linear absorption coefficient is

$$\mu(e, \mathbf{a}(t)) = \rho\mu_m(e, \mathbf{a}(t)) = (h^{-1})\frac{N}{s}N_a(\boldsymbol{\sigma}(e)\cdot\mathbf{a}(t)), \qquad (13)$$

where the functional arguments are clearly shown for $\mathbf{a}$ and $\boldsymbol{\sigma}$. Taking into account equation (13) and the Beer–Lambert equation we have

$$\exp\big(-A(e, t_i)\big) = \exp\left(-\frac{N}{s}N_a\big(\boldsymbol{\sigma}(e)\cdot\mathbf{a}(t_i)\big)\right), \qquad (14)$$

where each jth elemental atomic cross-section ($j = 1, \ldots$) is defined as follows: $\sigma_j(e) = f_{2,j}(e)/[(\pi/2)Ce]$ with the constant $C = 9.111 \times 10^{-3}$ (eV nm^2)$^{-1}$, where $f_{2,j}(e)$, the imaginary scattering factor for the jth atom at photon energy e, is taken from the X-ray database of the Centre for X-ray Optics, currently updated regularly by Eric Gulliksen (Henke *et al.*, 1993).

Equation (14) relates the optical density, the scalar product of the elemental atomic array and the elemental array of cross-sections for the ith pad,

$$A(e, t_i) = wN_a\big(\boldsymbol{\sigma}(e)\cdot\mathbf{a}(t_i)\big), \qquad (15)$$

where $w = N/s$ is a coefficient denoting the amount of material per area unit (mol cm^{-2}). In general, N and thus w both depend on the pad, *i.e.* the exposure time t. Unlike the more typically used expression, $h(e, t) = A(e, t)/\mu(e, t)$, equation (15) does not depend on the sample thickness or the sample density. Also, equation (15) demonstrates that the experimental optical density is proportional to the elemental array $\mathbf{a}$ with only one factor, w, which describes the number of moles per unit sample area, *i.e.* the areal molar density (or areal amount).

Equation (15) allows us to build a natural framework for obtaining the atomic composition of each pad (Section SI1.2). We assume that the n types of atoms constituting the particular ith pad which contribute most of the absorption are known. This defines the number of edges of interest and the components of the array $\boldsymbol{\sigma}$ from tabulated data. We then extract from the measured data a piecewise array of the experimental optical density functions $\mathbf{A}_i(\mathbf{e}, t_i) = (A_{1,-}(\mathbf{e}_-, t_i), A_{1,+}(\mathbf{e}_+, t_i), A_{2,-}(\mathbf{e}_-, t_i), A_{2,+}(\mathbf{e}_+, t_i), \ldots, A_{n,-}(\mathbf{e}_-, t_i), A_{n,+}(\mathbf{e}_+, t_i))$ constituting the *pre* $(-)$ and *post* $(+)$ parts for each of the n edges of the ith pad, where $\mathbf{e}_{(-\text{ or }+)} = (e_1, e_2, e_3, \ldots)$ denote the *pre*- and *post*-edge arrays of photon energies selected for fitting. Then, the elemental atomic array $\mathbf{a}$ of the given pad is derived through the following iterative process. The iterative process starts with the initial n components of the elemental atomic array $\mathbf{a}$, which contains values set arbitrarily at the beginning (Section SI1.2). Then, a linear least-squares fit is applied to the data $\mathbf{A}_i$ with respect to the given arrays $\mathbf{a}$ and $\boldsymbol{\sigma}$. In terms of the simplest function of the optical density $\mathbf{B_i}(\mathbf{e}, \mathbf{a}(t_i))$, the result is

$$\mathbf{B}_i\big(\mathbf{e}, \mathbf{a}(t_i)\big) = c + b\big(\boldsymbol{\sigma}(\mathbf{e}) \cdot \mathbf{a}(t_i)\big), \tag{16}$$

where b and c are the linear fit coefficients. This may not be the best fit for the given arbitrarily chosen $\mathbf{a}$. The quality of the fit for the ith pad is defined by the residual $R_i(\mathbf{A}, \mathbf{B}) = \mathrm{MSE}_i(\mathbf{a})$ and depends on $\mathbf{a}$ as a parameter, where MSE is the mean square error (Section SI1.2). The above iterative process repeats for the next elemental array $\mathbf{a}$ outputting the next corresponded $\mathrm{MSE}_i(\mathbf{a})$. The number of iterations depends on the number of permutations of the n components of the array $\mathbf{a}$, accounting for an increment of the change of the component values. Averaging the elemental arrays corresponding to the lowest residuals results the best elemental array $\mathbf{a}$, defining the direct components $a_1, a_2, \ldots, a_n$ for the ith pad. The above calculations were performed using *Mathematica* (WRI, 2020).

2.3. Obtaining densities $\rho_i(t)$ for each pad

The densities ρ_i of each pad can be calculated from the elemental atomic arrays $\mathbf{a}$. The fitting process outputs c and b coefficients for the best $\mathbf{a}$ (Section SI1.2). Here, $b = w$ and, thus, $b = N/s$. The density of the ith pad is

$$\rho_i = b_i\big(h_i^{-1}\big)(\mathbf{M}_\mathrm{r} \cdot \mathbf{a}_i), \tag{17}$$

where, on the right-hand side, all terms are known except the geometrical thicknesses h_i of the ith pad. If the topography of the 9-pad pattern is scanned by AFM, then the actual thickness h_i of the pads can be measured and all material densities of the pads can be calculated according to equation (17). If AFM data are not available, then equation (17) can deliver the areal density $\rho_i h_i$ instead, and analyze it with respect to the pad number (*i.e.* the dose applied).

2.4. Effect of irradiation dose caused by analytical study of the 9-pad pattern

Functions $A(e, t_i)$ and $\mu(e, t_i)$ are essential for calculating the dose imparted to the ith pad. This requires the pad to absorb some additional X-rays in order to measure OD images and spectroscopy stacks. It is important to minimize the analytical dose relative to the doses specifically applied to create the radiation damage. The total dose applied to each pad consists of two contributions, D_p, which is the dose of the 9-pad experiment and D_s, which is the dose from the spectroscopic analysis following the D_p experiment,

$$D = D_\mathrm{p}(e_D, t) + D_\mathrm{s}(e). \tag{18}$$

Ideally, the whole experiment – 9-pad dosing and the subsequent spectroscopic analysis – should be carried out such that D_s, the dose applied during analysis, is significantly less than D_p, the dose applied to generate the 9-pad pattern. In particular, the pad 1 gives the strictest condition and, ideally, $D_\mathrm{s} \ll D_1$. Although the doses for material damage may span three orders of MGy, the doses D_s, from the spectroscopic analysis, may be comparable with doses applied to pads 1, 2 and 3. From an analytical perspective, the first pads are important because they represent the fastest evolution of the optical density change (including μ change) with respect to the dose applied. Therefore, D_s must be calculated and included in the total dose D.

For calculating D_s equation (3) can be modified to remove time evolution (one of the models discussed below). The key criterion for such a simplifying assumption is $N_\mathrm{e} n \tau < t_1$, where n, N_e and τ are the number of edges, the total number of energies in the stack sequences and the dwell time. Under that condition, the total analytical exposure received by each pixel is less than the exposure received by the first pad. In this case μ and ρ do not depend on time and s and τ are constants for all edges. The total dose for all N_e analytical images is the sum of the dose received by the sample at each energy,

$$D_\mathrm{s} = \sum_{j=1}^{N_\mathrm{e}} \frac{e_j\, i_0(e_j)\, \mu(e_j)}{k(e_j)\rho s}\, \frac{1 - \exp\big(-A(e_j)\big)}{A(e_j)}\, \tau. \tag{19}$$

Examples of analytical NEXAFS spectra of the 3rd, 7th and 9th pad of a 9-pad pattern generated in PFSA at 320 eV are presented in Fig. 6. The calculations of D_p, D_s, density and composition at each pad were performed using *Mathematica* (WRI, 2020) – see Table S7. As is shown below, in this particular study it was possible to measure the required spectra using a total D_s of ~1 MGy, which is an order of magnitude smaller than D_1, the dose for pad 1.

3. Experimental

3.1. Sample preparation

The PFSA studied is a commercial 5% alcohol-based dispersion of Nafion$^\mathrm{TM}$ D521 (equivalent weight = 1100; Ion Power Inc.), with the solvent consisting of 45 ± 3 wt% water, 48 ± 3 wt% 1-propanol, <4 wt% ethanol, <1 wt% mixed ethers. The uniform thin film samples used for STXM were prepared by spin coating the commercial dispersion diluted to 4% using isopropanol (IPA) (99.5%, Caledon Laboratory Chemicals). The diluted dispersion was ultrasonicated for 5 min to ensure complete mixing. Then a drop was deposited

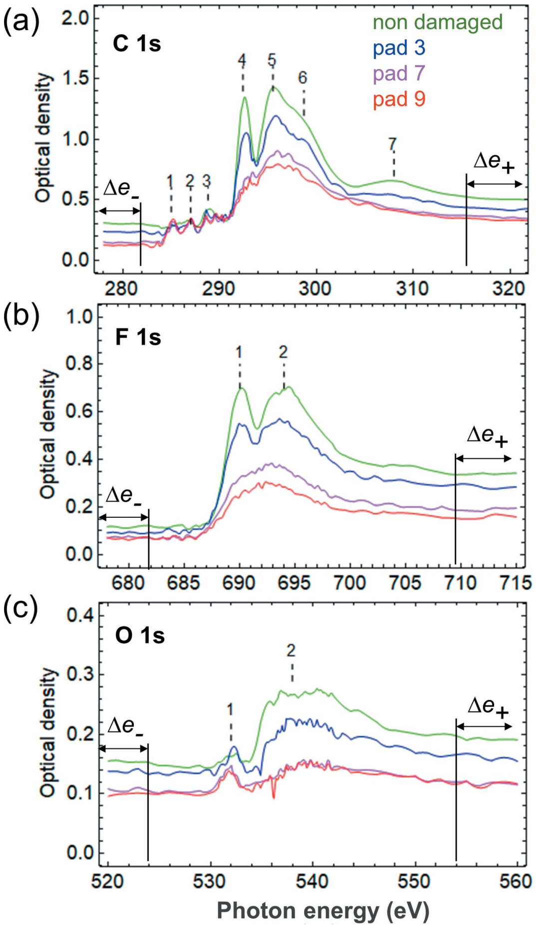

Figure 6
NEXAFS spectra of PFSA(1100) recorded from a 9-pad dose-damage experiment. Panel (*a*) corresponds to the C 1*s* edge, (*b*) to the F 1*s* edge and (*c*) to the O 1*s* edge. The color coding of spectra corresponds to the color of the boxes in Fig. 4(*c*). The pre-edge and post-edge intervals selected for the elemental component fitting are shown as Δe_- and Δe_+, respectively. The peaks, energies and assignments are presented in Table S4.

on the surface of a 10 mm × 10 mm piece of freshly cleaved mica, placed on the rotor of the spin coater (6708D, Specialty Coating Systems). The coating was created using a spinning rate of 4500 r.p.m. for 30 s at ambient temperature and pressure. Film thicknesses (measured by STXM) were ~150 nm, with small variations depending on the concentration of the diluted dispersion. After spinning, the film was not annealed. Squares of ~1 mm^2 were gently drawn on the coated mica surface using a fresh scalpel blade. Then the piece of mica was inserted at a 45° angle (coated surface up) through the surface of distilled water. Water capillary forces separate the polymer thin films from the mica surface, allowing them to float on the water surface. The floating polymer films were then transferred either to SiN$_x$ windows (5 mm × 5 mm frames, 1.0 mm × 1.0 mm windows, Norcada, Inc), Fig. 4, or to bare TEM grids. Care was taken to position the polymer film such that a part of the SiN$_x$ support was uncovered providing an area for measuring the i_o signal important for STXM data processing, Figs. 4(*b*) and 4(*c*).

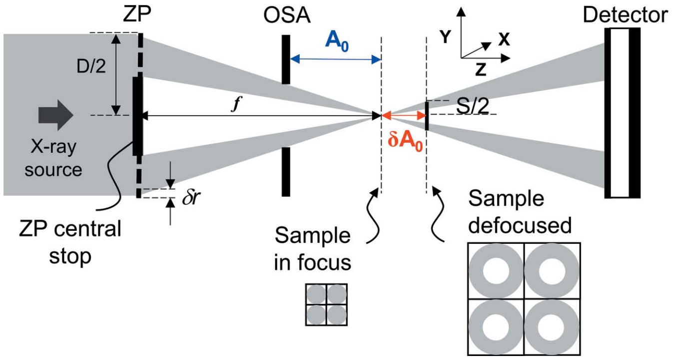

Figure 7
Schematic of STXM optics indicating how the position of the ZP relative to the sample affects the spot size on the sample. *D* is the width of the ZP, OSA is the order-sorting aperture, A_0 is the position of the sample relative to the OSA, δr is the width of the ZP outer zone and δA_0 is the value added to A_0 to set the position of the ZP to achieve a desired spot size *S*. Beam layouts at the sample for each of four adjacent pixels are shown for the sample positioned to be 'in focus' and 'defocused'.

3.2. Scanning transmission soft X-ray microscopy (STXM)

The ambient STXM on beamline 10ID1 at the Canadian Light Source (CLS) (Kaznatcheev *et al.*, 2007) was used for 9-pad generation and analysis. STXM instrumentation, data acquisition and analysis methods have been presented elsewhere (Kilcoyne *et al.*, 2003; Ade & Hitchcock, 2008; Hitchcock, 2012). All raw data were analyzed with *aXis2000*.[4] Briefly, the same monochromator grating (low-energy grating, 250 lines mm^{-1}) was used for collecting data at the C 1*s*, O 1*s* and F 1*s* edges. A monochromatic X-ray beam is focused on the sample and the sample is (x, y) raster-scanned while the transmitted X-ray intensity is recorded using a single-photon-sensitive X-ray detector, consisting of a phosphor (P43) powder to convert each X-ray into a shower of visible photons, which are detected with a high-performance photomultiplier tube, PMT (Hamamatsu R647), Fig. 7. The fully focused beam diameter and hence the spatial resolution, Δx, is determined by the width of the outer zone, δr, of the zone plate (ZP), $s \simeq 1.22\delta r$ (Attwood & Sakdinawat, 2017). Measurements typically used a ZP with δr = 25 nm, ZP diameter = 240 µm and a central stop diameter of 90 µm. The detector efficiencies, which were measured using the lithography transition of PMMA (Leontowich *et al.*, 2012), are presented in Section SI2. The relative (x, y) positions of the sample and the ZP are controlled by interferometry using the fast-piezo scanning stage to maintain the relative sample–ZP lateral position within ~10 nm with ~1 kHz response. The SiN$_x$ windows with the polymer thin film samples were attached to STXM sample holder plates by carbon or double-sided tape and the holder was then loaded on the three-pin kinematic mount in the STXM chamber. For the majority of experiments the STXM chamber was first evacuated to ~10 Pa and then back-filled with ~15 kPa of He. The energy scales were calibrated using the C 1*s* → 3*s* transition of CO$_2$ gas at 292.74 eV (Ma *et al.*, 1991).

---

[4] *aXis2000* is written in Interactive Data Language (IDL). It is available free for non-commercial use from http://unicorn.mcmaster.ca/aXis2000.html.

For each photon energy measured, the transmission image is converted to optical density, $A(e)$, using Beer–Lambert's law: $A(e) = \ln(i_0(e)/i(e))$, where i_0 is the transmitted intensity without the sample but through all other materials at the position of the sample (windows, substrate, filters, *etc.*), and i is the intensity transmitted through the sample for the position (x, y). Analytical images and image sequences, also called stacks (Jacobsen *et al.*, 2000), were acquired at the C 1*s*, O 1*s* and F 1*s* edges.

3.3. Soft X-ray damage generation by STXM

Radiation damage was created using a photon energy of 320 eV in the C 1*s* continuum. The pattern generation routine (*Pattern Gen*) in *STXM_Control* (Kilcoyne *et al.*, 2003) was used to irradiate the sample film in a 9-pad array pattern consisting of 3 × 3 square pads, with each pad exposed for different dwell times, Fig. 4(*c*). A non-linear sequence of the dwell time was used with base values of (0.025, 0.05, 0.075, 0.125, 0.25, 0.375, 0.5, 0.75, 1.0) ms which was then modified at execution by a time multiplier, TM. To adjust the dose to the range of interest, the time multiplier coefficient, TM, was set to 10^4 for the presented data, which exposed each point in the 9th pad to the defocused (~180 nm diameter) X-ray beam for 10 s.

In the 9-pad pattern each pad is generated by a square array of 10 × 10 exposure points (pixels). For this study, a defocused beam was used with 180 nm pixel–pixel spacing, so that the individual pads were ~2 µm × ~2 µm and the set of 9 pads fit into an area of 10 µm × 10 µm. In order to distribute the radiation uniformly over each pad with complete area filling but without overlap, the beam diameter s at the sample was set to be equal to the pixel spacing by defocusing the beam using an offset, δA_0, to A_0, the OSA–sample distance along the optical axis. The parameter δA_0 which gives a beam diameter of s is calculated from $\delta A_0 = E\delta r s/1240$, where E (eV) is the photon energy, δr (nm) is the width of the ZP outer zone, and the constant 1240 has a dimension of (eV nm). In practice, to set a given defocus, first a sharp focus must be determined and the correct A_0, for that focus set. Then the A_0 value for in-focus imaging is adjusted to be $(A_0 + \delta A_0)$ to achieve the desired defocused beam diameter s (Fig. 7). From a geometrical perspective, at values of s above ~100 nm the defocused beam spot becomes an annulus because of the ZP central stop (Fig. 7). However, due to diffraction and secondary electron migration there is spatial spreading of the damage (Wang, Stöver *et al.*, 2007; Leontowich *et al.*, 2011, 2012) such that the annulus shape is only seen clearly for much larger beam diameters. For PFSA, we have observed the annulus shape of the beam only when using a defocus greater than 500 nm (Martens *et al.*, 2019).

4. Results

Fig. 4(*c*) presents a STXM OD image at 690 eV of the 9-pad pattern generated in PFSA which is used to illustrate the method. For PFSA, the energy of 690 eV provides the best contrast (absorption difference between the damaged and non-damaged areas). The area average values of optical densities, A, taken at 320 eV, e_D, for each pad with respect to the exposure time, t, are presented in Fig. 8. This set of data is least-squares fit to two models. Note, these models are ways of reducing the measured data to a few parameters, but do not include the considerations that are the main thrust of this paper. The fits are presented in Section SI3. The details and validity of the fit models have been discussed elsewhere (Berejnov *et al.*, 2018). Model 1 (solid line in Fig. 8) is an exponential, $A(t) = c_1 + a_1\exp(-b_1 t)$, which is the 'traditional' fitting model for treating cases without mass loss, chemical change or density changes (Wang, Morin *et al.*, 2009). Model 2 (dashed line in Fig. 8) is a hyperbolic function, $A(t) = c_2 + a_2/(b_2 + t)$, a model that was recently introduced (Berejnov *et al.*, 2018). The fitting coefficients for both models and the mean square errors of the fits are presented in Table S3.1. The coefficient c in both models corresponds to the asymptotic values of optical densities at infinite exposure time $A(t \to \infty)$, $c_1 = 0.34$ and $c_2 = 0.32$, respectively. Both models provide a fitting quality acceptable for the present demonstration of the method, although the hyperbolic fit is statistically better for the given experimental data.

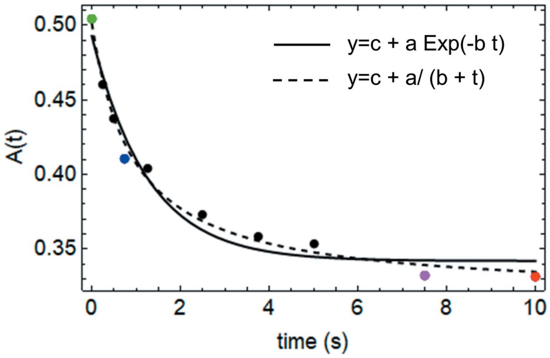

Figure 8
Optical densities $A(t)$ for all pads of the 9-pad damage experiment on PFSA(1100) (Nafion$^{\rm TM}$ D521) including the non-damaged area taken at 320 eV (damage energy). The color coding of points corresponds to the color of the boxes in Fig. 4(*c*). The curves correspond to the linear least-squares fittings according to model 1 (solid) and model 2 (dashed), see Sections SI3.1 and SI3.2.

NEXAFS spectra were measured for the whole 9-pad experimental area [Fig. 4(*c*)] using about 100 energy points in the 30–40 eV energy intervals at each of the C 1*s* (280–320 eV), O 1*s* (524–560 eV) and F 1*s* (680–720 eV) edges, see Fig. 6. Assignment of the fine-structure peaks is presented in Table S4 and has been discussed in detail elsewhere (Yan *et al.*, 2018). The average NEXAFS spectrum of each pad was extracted and the spectra from the three edges appended to generate a single 280–720 eV spectrum for each pad. Then the pre-edge (−) and post-edge (+) intervals were saved and the fine-structure intervals were removed for each edge for the entire data set producing the piecewise array of the experimental optical density functions $\mathbf{A}_i(e) = (A_{\rm C,-}(e, t_i), A_{\rm C,+}(e, t_i), A_{\rm O,-}(e, t_i), A_{\rm O,+}(e, t_i), A_{\rm F,-}(e, t_i), A_{\rm F,+}(e, t_i))$ where i denotes the particular pad.

Table 1
Composition of all pads including the non-damaged area defined by coefficients of the elemental array **a** for S, C, O, F and H.

Parameters of fitting and areal density (g cm^{-2}) and estimated thickness (nm) of each pad and the undamaged material.

	Elemental array **a**						LLS fitting†			
Pad *n*	S	C	O	F	H	MSE‡	*c*	*b*	Areal density§ (1×10^{-5} g cm^{-2})	Thickness¶ (nm)
0††	2.7	22.6	8.1	41.7	1.0	1.1×10^{-5}	7.96×10^{-3}	0.246	3.15	158
1	2.3	22.4	7.7	40.2	1.0	1.1×10^{-4}	1.68×10^{-2}	0.233	2.87	143
2	2.1	23.5	6.9	40.0	1.0	7.5×10^{-5}	1.39×10^{-2}	0.219	2.69	134
3	1.9	23.9	6.4	39.8	1.0	4.4×10^{-5}	1.37×10^{-2}	0.210	2.55	127
4	1.8	24.5	6.7	37.1	1.0	4.2×10^{-5}	1.07×10^{-2}	0.205	2.4	120
5	1.4	23.4	5.0	31.6	1.0	3.5×10^{-5}	1.00×10^{-2}	0.210	2.12	106
6	1.2	22.9	4.2	28.3	1.0	2.5×10^{-5}	1.16×10^{-2}	0.204	1.89	95
7	1.1	23.7	4.2	28.4	1.0	3.0×10^{-5}	8.62×10^{-3}	0.197	1.85	93
8	1.2	23.4	4.2	24.1	1.0	2.8×10^{-5}	8.96×10^{-3}	0.195	1.66	83
9	1.0	24.8	5.0	22.4	1.0	3.2×10^{-5}	5.10×10^{-3}	0.193	1.62	81

† LLS is the linear least squares. *c* and *b* are the least-square-fitting constants in equation (16). ‡ MSE is the mean square error of the fit in equation (S6). § From Fig. 12. ¶ Thickness = 100 × (areal density in 10^{-5} g cm^{-2}) / (density in g cm^{-3}), assuming d = 2.0 g cm^{-2} for all pads, see Section SI9. †† Pad 0 is from an area not intentionally damaged.

The iterative procedure (Section SI1.2) of obtaining the elemental array **a** corresponding to the best fit of $\mathbf{A}_i(e)$ to the scalar product $\boldsymbol{\sigma}(e) \cdot \mathbf{a}(t_i)$ was applied for each pad. The graphical results of the fits to the non-damaged area and for pads 3, 7 and 9 are presented in Fig. 9 while graphs for all 9 pads are presented in Section SI5. The numerical compositions of all elemental arrays **a**, the least-square fit coefficients *b* and *c* [according to equation (16)], and the corresponding mean square errors [according to Section SI1.2, equation (S6)] are presented in Table 1.

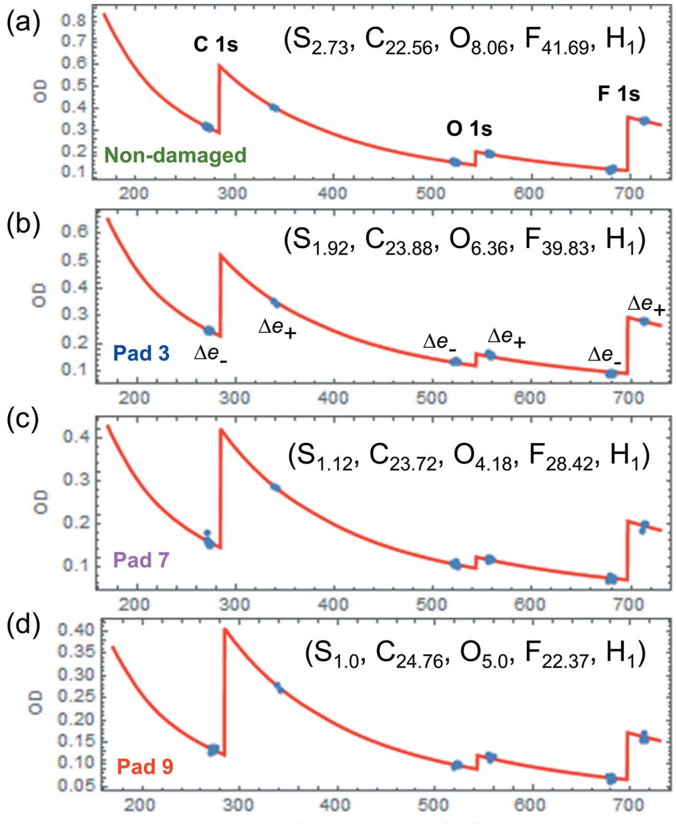

Figure 9
Linear least-squares fitting of the pre- and post-edge intervals (indicated by blue points) of C 1*s*, O 1*s* and F 1*s* edges NEXAFS spectra with respect to the best-found composition of the elemental array **a**. Fitting is presented for four different areas: (*a*) non-damaged, (*b*) pad 3, (*c*) pad 7 and (*d*) pad 9. The spectra of all 9 pads are presented in Fig. S5. Note the vertical scale differs for each pad.

The material examined, Nafion$^{\rm TM}$ D521, is a long-side-chain (LSC) fluoropolymer with an equivalent weight (EW) of 1100 g mol^{-1} denoted as PFSA(1100) for short. For LSC fluoropolymers the atomic composition of the molecular unit is defined by the following expression: S[1] C[7 + 2*m*] O[5] F[13 + 4*m*] H[1], where $m = (\mathrm{EW} - M_r(\mathrm{unit}))/M_r(\mathrm{C_2F_4})$ (Mauritz & Moore, 2004). For LSC fluoropolymers the molecular mass of the repeat unit is $M_r(\mathrm{unit})$ = 444 g mol^{-1} and $M_r(\mathrm{C_2F_4})$ = 100 g mol^{-1} giving m = 6.56. Therefore, the atomic composition of the undamaged PFSA is **a** = (1, 20, 5, 39, 1); see Section SI6 for elemental order in the array. For the iterative fitting procedure, the number of H atoms per repeat unit was always set to 1. The number of S atoms per repeat unit in each pad was used as a fitting parameter (Section SI6).

Fig. 10 plots the evolution of the atomic composition as a function of exposure time due to radiation-damage-induced mass loss. Fig. 10(*a*) shows the elemental atomic arrays **a** with respect to the exposure time applied. The black points denote the components of the target array **a** for undamaged PFSA(1100). Despite the shortness of the photon energy intervals of the pre- and post-edges (*i.e.* limited number of experimental points selected for the fit) the overall fit of the elemental array **a** for the non-damage area of PFSA(1100) is pretty close to the target values. Fig. 10(*b*) shows the molecular weight of the elemental atomic array for each pad with respect to the exposure time applied.

Elemental linear absorption coefficients were calculated for each pad from the formula

$$\mu(e, \mathbf{a}) = \rho N_a (\boldsymbol{\sigma} \cdot \mathbf{a}) / (\mathbf{M}_r \cdot \mathbf{a}). \qquad (20)$$

The elemental atomic arrays are those reported in Table 1. The material density ρ of PFSA(1100) is assumed to stay constant (for illustration only) and equal to 2.0 g cm^{-3}. We

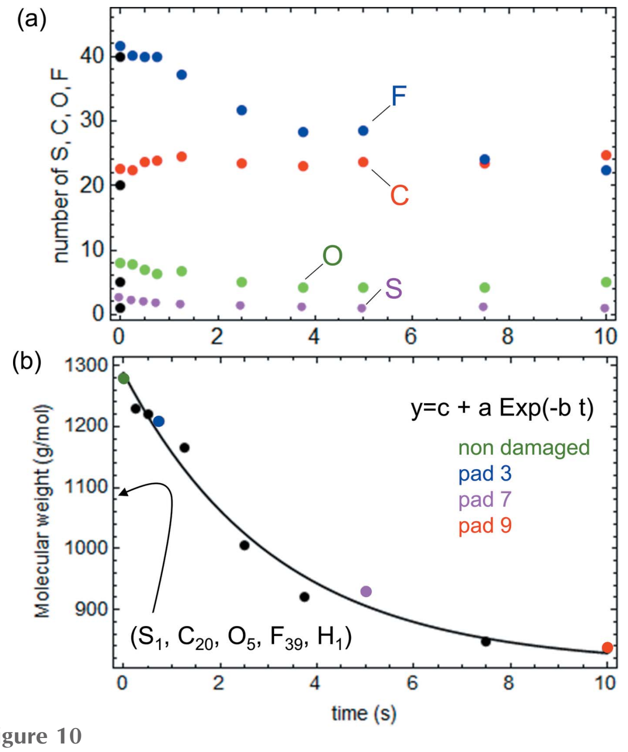

Figure 10
Evolution of the elemental atomic composition corresponding to the pad's material with respect to the exposure time. Panel (*a*) plots the number of each element – S (pink), C (red), O (green) and F (blue) – as a function of pad number, as expressed by its exposure time. Black points correspond to the non-damaged PFSA(1100) composition. Panel (*b*) plots the derived molecular weight of the formula unit of the *i*th pad ($\mathbf{M}_r \cdot \mathbf{a}_i$) with respect to exposure time. The color coding of points corresponds to the color of the boxes in Fig. 4(*c*). The arrow depicts the target molecular weight for non-damaged PFSA(1100). The solid curve is an exponential fit (see Section SI8).

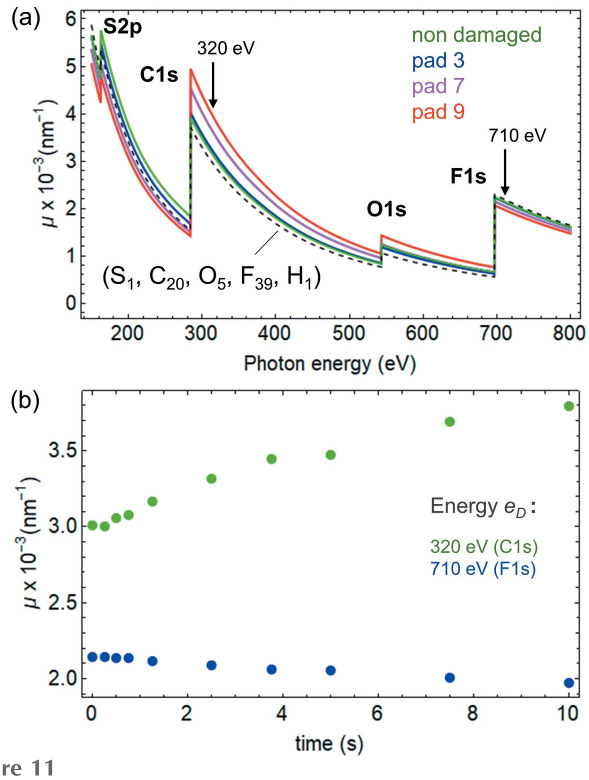

Figure 11
(*a*) Linear absorption coefficients $\mu(e, \mathbf{a})$ for the non-damaged area and pads 3, 7 and 9. The colors correspond to Fig. 4(*c*). The dashed black curve corresponds to the non-damaged PFSA(1100) with a target elemental atomic array of (1, 20, 5, 39, 1). Arrows indicate the dose energies: 320 eV (used to generate the data analyzed in this article) and 710 eV (a suitable alternative). (*b*) Time (dose) evolution of the linear elemental absorption coefficient at dose energies used at the C 1*s* edge (320 eV) and at the F 1*s* edge (710 eV).

note that, if the pad thickness was measured, then the actual density of each pad could be determined with this method.

Fig. 11(*a*) plots the derived S, C, O and F elemental linear absorption coefficients for undamaged PFSA(1100) and selected damage pads (3, 7, 9). Over the dose regime measured, the highest variation of the linear absorption coefficient is $\sim 1.0 \times 10^{-3}$ (nm^{-1}) at the C 1*s* edge, while the smallest variation is $\sim 2.0 \times 10^{-4}$ (nm^{-1}) at the F 1*s* edge. Fig. 11(*b*) plots the changes in μ at 320 eV and 710 eV as a function of time. This plot shows the rather puzzling result that, despite very little change in the number of carbon atoms (20 → 24) and extensive decrease in the number of fluorine atoms (40 → 25), μ(320 eV) changes much more than μ(710 eV). This seems to be a direct contradiction to the measured absorption spectra (Fig. 6) which show very little change in the C 1*s* edge jump [OD(320 eV)–OD(280 eV)] with time/damage, but an enormous reduction in the F 1*s* edge jump [OD(710 eV)–OD(680 eV)], indicating a huge loss of fluorine but negligible change in the amount of carbon. However, this can be understood by noting that there is a large reduction in the areal density over the damage series (Fig. 12), calculated as $\rho_i h_i$ using equation (17). Since the absorbance, $A_i = \mu_i \rho_i h_i$, is the product of the derived elemental linear absorption coefficient and the areal density, the derived μ_i and areal density $\rho_i h_i$ for each damage pad and for the non-damaged area are consistent with the measured optical density spectra, as shown in Fig. S9 and discussed in Section SI9 of the supporting information.

Fig. 13 plots the dose at each pad calculated using four different methods of the dose evaluation discussed in the *Introduction*. The simplest model (Dose 1, green) assumes that

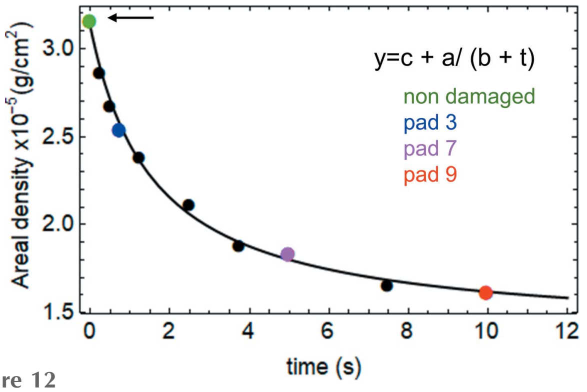

Figure 12
Areal density plotted as a function of exposure time. The colors correspond to Fig. 4(*c*). The arrow indicates the point corresponded to the non-damaged PFSA(1100) with a targeted elemental composition (S_1, C_{20}, O_5, F_{39}, H_1), density of 2.0 g mol^{-1} and 150 nm thickness. The solid curve is a hyperbolic fit (see Section SI8).

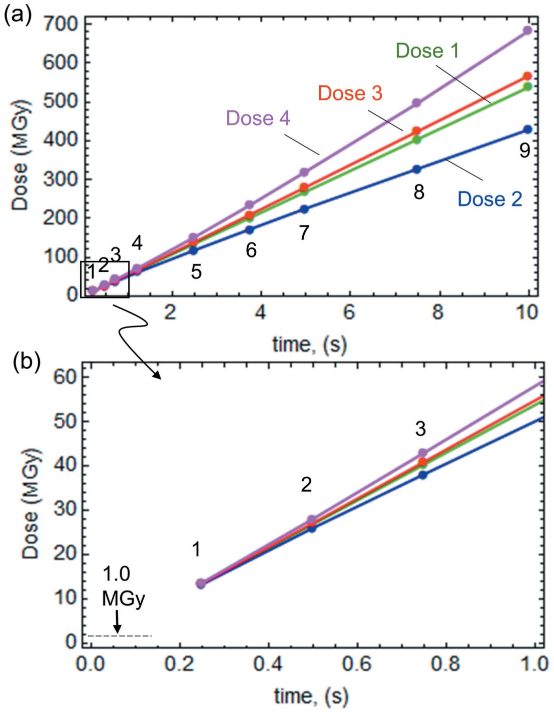

Figure 13
Dose as a function of exposure time for each pad, calculated according to four different dose models. The numbers at each point denote the pads. Dose 1 denotes model 1 (dose resistive material), dose 2 denotes model 2 (mass resistive material), dose 3 denotes model 3 (linear absorption coefficient and density resistive material) and dose 4 denotes the present model where there is no restriction with respect to changes in material chemistry or elemental composition. Panel (*b*) shows an expanded view of the low dose regime, indicated by the solid box in (*a*). The dashed line in (*b*) denotes 1 MGy dose, the maximum value of the dose that the sample experienced from the C 1*s*, O 1*s* and F 1*s* NEXAFS analytical studies of the 9-pad pattern.

radiation damage does not change the material, Fig. 1(*a*). The second model (Dose 2, blue) assumes that the pattern in Fig. 4(*c*) is due to optical density change only, Fig. 1(*b*), The third model (Dose 3, red) represents the case, Fig. 1(*c*), where changes of the optical density and the mass at each pad are taken into account but assumes that both are decaying due to removal of the molecular units constituting the film material (*i.e.* the Dose 3 model assumes that material density and material linear absorption coefficient are the same for all pads). The fourth model (Dose 4, magenta) treats each pad as having its own chemistry, composition, linear absorption coefficient and mass per area. Fig. 13(*b*) presents the doses calculated by each of the four models for pads 1, 2, 3, those with low exposure, illustrating that, if the doses are low, then all models give very similar results.

The doses, $D_{\rm s}$, received by the sample due to recording the full stacks for the C 1*s*, O 1*s* and F 1*s* edge were calculated according to equation (19) and are summarized in Table S7. Equation (19) was used for selected energies and pixel sizes to calculate the dose per specific OD image. Each OD image used for analysis (those are taken at 292.4, 320 and 690 eV before and after the pad generation) added <0.01 MGy, while imaging during navigation added <0.001 MGy. As noted above, the analysis dose is much smaller (<1 MGy) than the dose used to generate pad 1 (∼10 MGy).

5. Discussion

The 9-pad experiment, where each area (a pad) is receiving an incrementally increasing dose starting from undamaged material, is a common practice for studying the effect of radiation on materials. The current analytical treatment of the 9-pad data assigns to each pad the material properties which the pad has at the end of its radiation exposure. As a result, the final state of the material of the pad is attributed to the entire lapsed time of exposure, *t*. In cases where the irradiated material changes significantly, the parameters entering the dose calculation μ, ρ and A in equation (2) become the functions $\mu(e_D, t)$, $\rho(t)$ and $A(e_D, t)$. In order to calculate the dose delivered to each pad those functions must be defined, *i.e.* approximated, for all 9 intervals of integration. We proposed a different way of calculation – partitioning. Although it may seem a bit cumbersome, it bypasses the functional approximation step. The method uses the fact that each pad experiences an irradiation that combines that already delivered to the previous pad with an additional dose. In this case we can construct a simple and recursive calculation procedure, equations (10) and (11), each time taking into account the discrete values for μ_i, ρ (from fitting) and A_i (from experiment). The integration of equation (2) becomes a series of algebraic terms. In the current example we used so-called rectangular partitioning for the sake of demonstration. A more accurate procedure would be to use trapezoidal partitioning (Atkinson, 1989).

The presented method, in contrast to earlier approaches, also provides fundamental insights for differentiating and understanding the effects of different types of damage. The damage is quantified in terms of optical density change $A(t) = \mu(t)h(t)$, where all parameters are functions of the exposure time *t*. This approach involves two damage characteristics. The maximum change of A quantifies the maximal damage, which can be used as a scale for normalizing $A(t)$. The change of optical density with respect to the increment of exposure time $\Delta A(t)/\Delta t$ quantifies the damage rate. Both characteristics can be derived from data similar to that presented in Fig. 8 by applying the analysis outlined in Sections SI3.1 and SI3.2. Note, in this approach the choice of $A(t)$ functionality was arbitrarily selected as exponential. However, neither the maximal damage nor the damage rate can clarify the origin of the damage in the generic case considered in this paper. Questions such as 'which element (or chemical bonding motif) is most damage prone?', 'which is less?', and 'does the damage cause selective elemental loss or molecular unit ablation?', are behind this approach. The presence of such uncertainty is because the optical density, A, is a product of the linear absorption coefficient $\mu(t)$ and the sample thickness $h(t)$, which in turn are functions of other variables, *i.e.* they are not fundamental. Therefore, the analysis of only $A(t)$, as plotted in Fig. 8, is insufficient for a clear understanding of the fundamental aspects of radiation damage to a given material.

The method presented in this paper resolves the above ambiguity. Equation (15) shows that the optical density $A = wN_a(\boldsymbol{\sigma}\cdot\mathbf{a})$ is a function of two independent variables only, the elemental array **a** and the number of molecular units per area of the sample, w. Those variables describe the properties of the material and cannot be reduced further, *i.e.* they are fundamental. Other variables can be derived from **a** and w. For example, if one can measure the thickness, h, then the dose-dependent bulk density $\rho = w(h^{-1})(\mathbf{M}_r\cdot\mathbf{a})$ and the linear absorption coefficient $\mu = w(h^{-1})N_a(\boldsymbol{\sigma}\cdot\mathbf{a})$ can be derived.

Further, fitting A to generate **a** and w provides a logical decoupling of different intrinsic aspects of the radiation damage presented in Figs. 10 and 12. These figures represent two distinct types of the damage to PFSA: the change of the elemental composition of the molecular unit (Fig. 10), and the change of number of molecular units in the irradiated area (Fig. 12). The change of composition due to irradiation could be quite complex – compare the evolution of elemental composition in Fig. 10(*a*).

Interesting insights into PFSA damage mechanisms can be obtained from the types of mathematical functionalities which best approximate the effective molecular mass of the material unit and the areal density. We found that M_r (*i.e.* **a**) can be approximated with *exponential* functionalities (Section SI8.1) and the quality of that approximation is better when the time of exposure is higher, indicating that there are at least two regimes corresponding to short and long exposure time intervals. The probable existence of more than one damage regime for PFSA has been discussed previously (Melo, 2018). Note, the hyperbolic functionality does not fit M_r, see Fig. S8.1. However, the change of the areal amount of material, w (*i.e.* areal density, ρh), can be approximated by a *hyperbolic* function and the quality of that approximation also increases with increased exposure time (see Fig. S8.2). Therefore, two parameters with different functionalities, $w(t)$ – hyperbolic – and $\mathbf{a}(t)$ – exponential, contribute to the same optical density $A(t)$. As a result, $A(t)$ can exhibit either type of these two functional dependences. The dominant one depends on which term is more important with respect to the chosen material and how this material reacts to the applied radiation. In this context, the term 'critical dose', which is used extensively in current discussions of radiation damage (Coffey *et al.*, 2002; Wang, 2008; Wang, Morin *et al.*, 2009) and involves an exponential fit to $A(t)$, may not have a generic meaning. Extrapolating the above observation, one can conclude that, if an exponential model is found experimentally to provide a good fit to $A(t)$, this indicates that, for the chosen experimental conditions, the decay of optical density with increasing dose is mainly controlled by changes of the elemental array **a** while there is little change in w, the number of the effective molecular units per sample area. This may explain why the exponential approximation is frequently found to be a poor fit to experimental $A(t)$. However, this intriguing observation needs to be verified for different materials and different conditions.

Our procedure depends on the accuracy of the method for determining the elemental array **a**. The experimental data and their fit, Fig. 9 (Section SI5) and Table 1, indicate a fitting accuracy (standard deviation) of 2% or lower. Thus 2% is an upper bound to the accuracy of array **a**. The accuracy can be further improved by adding more points in the pre- and post-edge intervals, and by adding more edges. These changes would further reduce the value of the constant, c, which is an absorbance offset at each edge, equation (16).

Regarding the material properties, the elemental array of the *undamaged* material is not in perfect agreement with the *target* elemental array (1, 20, 5, 39, 1) that one calculates for PFSA(1100) using the formulae provided by the manufacturers (Mauritz & Moore, 2004). Fig. 10(*a*) shows that the number of each element in the polymer unit of the undamaged material (2.7, 22.6, 8.1, 41.7, 1) is systematically higher by ∼3 atoms per element than expected for the target (the calculated residual array is $S_{1.7}C_{2.6}O_{3.1}F_{2.7}$). This gives a noticeable increase relative to the molecular mass of the formula unit (S = 54.4; C = 31.2; O = 49.6; F = 51.3) giving in total ∼187 g mol^{-1} of additional molecular mass. The molecular masses of the undamaged and target materials are 1281 and 1094 (g mol^{-1}), respectively, Fig. 10(*b*). How can we understand this difference? The current state of molecular characterization of PFSA does not provide a direct measure of the molecular mass (Mauritz & Moore, 2004) due to an inherent inability to produce good (mono-molecular) solutions suitable for chromatographic study. Instead, the mass is evaluated by an indirect method in which the molecular formula is estimated from the ionic exchange capacity, which is a metric of available sulfonic groups in the material, and is the reciprocal of the EW of PFSA (Mauritz & Moore, 2004). This method is not precise, and it is widely accepted by manufacturers that an interval of ∼200 (g mol^{-1}) is a usual variance for the EW (g mol^{-1}) of ionomers like Nafion$^{\text{TM}}$ (LSC). Taking into account the EW uncertainty, the molecular masses derived by both methods (X-ray absorption and ionic exchange capacity) are not dramatically different. It is worth mentioning that, as opposed to the current state of PFSA characterization, X-ray absorption spectroscopy is a *direct method*. Potentially it can deliver the absolute elemental composition of the formula unit of PFSA once the X-ray absorption at each edge is calibrated with some appropriate standard samples. We did not elaborate this stream of research and used PFSA material as an illustrative example of our method of dose calculation.

It is also important to note that for the given demonstration all elemental characterizations of the material of the pad should be considered as being *effective*. Indeed, the present method employs X-ray transmission and therefore the damage is not uniform through each pad, but rather is larger at the upstream side than the downstream side of the PFSA film. The lack of sampling along the X-ray beam propagation direction could be remedied if one used STXM tomography (Wu *et al.*, 2017; Wu, Zhu *et al.*, 2018). Once transmission STXM stacks are measured at multiple tilt angles and the above method is applied to each voxel derived from a tomographic reconstruction of the tilt series data (rather for the entire pad volume), then the elemental material change could be evaluated on a much smaller volume, which could then track changes through the thickness of the sample layer.

Fig. 13 plots the dose at each pad calculated using four different methods. The simplest model (Dose 1, green) assumes that radiation damage does not change the material, Fig. 1(*a*), which is clearly not the case (see Fig. 4(*c*) demonstrating a clear damage pattern) but is included here for reference. This model results in a significant underestimate of the dose. For computing the dose for this model, it was assumed that the optical density does not change with exposure time and is that of the non-damaged area. This simplification is popular for fast dose estimation and allows the time integral T in equation (3) to reduce to the product of its integrand on the exposure time t.

The second model (Dose 2, blue) assumes that the pattern in Fig. 4(*c*) is due to optical density change only, and ignores changes in composition or areal mass. For this model the time integral T cannot be reduced to the product of the equation (3) integrand on the exposure time t. Thus, T must be calculated either analytically or by partitioning the interval of integration. This model also does not explain the case in Fig. 4(*c*), and is included here for reference. The curve for the Dose 2 model is below that for the Dose 1 model because the integrand $1 - \exp(-A(x))/A(x)$ in equation (2) is a decaying function with x, while for the Dose 1 it has a constant value. Integrating the constant will give a higher dose for large enough time.

The third model (Dose 3, red) represents the case where changes of the optical density and mass at each pad are taken into account but assumes that both are decaying due to removal of intact molecular units constituting the film material (*i.e.* the Dose 3 model assumes that material density and material linear absorption coefficient are the same for all pads). According to this model all pads in Fig. 4(*c*) should have very similar NEXAFS spectra, which is not the case (Fig. 6). Therefore, the Dose 3 model also should not be used. It is curious that the Dose 1 model is closer to the Dose 3 than the Dose 2 model, *i.e.* it gives more ‘accurate’ dose values than the Dose 2 model, despite the use of less appropriate assumptions.

The fourth model (Dose 4, magenta) treats each pad as having its own chemistry, composition, linear absorption coefficient and mass per area. Of the four models presented, Dose 4 is considered to be the most accurate since it uses most of the STXM data and has fewer assumptions. The fact that we assume a constant density in our calculations only reflects a limitation of our experimental measurements (no AFM data) rather than model limitations. Note, the Dose 4 model gives *higher* doses than the Dose 3 model with a noticeable difference. The Dose 3 model is already taking into account the fact that the thickness (and thus mass) changes with damage in proportion to the optical density, but it ignores the change in material composition. When the dose is applied at the particular energy, the material change represented by the linear absorption coefficient change, Fig. 11(*b*), could be *positive* and significant. Taking this into account in the integrand of equation (2) gives an overall dose higher than for the Dose 3 model. Note, the above conclusion is photon-energy-sensitive, see Fig. 11(*b*). The figure presents an example of the linear absorption coefficient taken for 710 eV – this energy also could be used for dosing. At 710 eV the change is low and *negative*, considerably different than at 320 eV.

Fig. 13(*b*) presents the doses for pads 1, 2 and 3, those with low exposure, illustrating that if the doses are low then all models give similar results. Below the calculated dose for pad 1, the dose is so low that there is no sense to deviate from the Dose 1 model. Experimental proof of this would be the absence of a detectible 9-pad pattern generated with TM = 50 and the defocused beam used in this study.

The full stack analytical study (Table S7) for all C 1*s*, O 1*s* and F 1*s* edges added about $D_{\rm s} \simeq 1$ MGy, which is negligible compared with the intentional doses used to create analyzable radiation damage, see the dashed line in Fig. 13(*b*). For comparison, pad 1 received $D_{\rm p} \simeq 14$ MGy.

The following improvements could be considered for future dose- and damage-related experiments. Detailed spectroscopic data with 100–200 energy points per edge is important for qualitative and fast analysis of the damage of the material under study. However, the pre- and post-edge fitting for multiple edges requires significantly less energy points. In this study we used $\sim$5 points for each pre- and post-interval per edge. This number could be changed depending on the particular signal/noise ratio. It is important to make sure that intervals are selected on the energy scale to properly match the pre- and post-edges and that the total dose of the pre-post edge spectroscopic analysis is very low, preferably below 1 MGy. It is also worth considering ways to explicitly study the kinetics of the through-layer damage propagation, which might be performed using STXM spectro-tomography.

6. Conclusion

Accurate determination of the dose imparted to a material by soft X-ray absorption requires knowing the type of radiation damage that material undergoes. Depending on how the material changes on X-ray irradiation the appropriate type of dose calculation must be used. The 9-pad experimental protocol together with NEXAFS spectroscopy (and AFM) is a convenient tool for analyzing the type of radiation damage, and for obtaining the material properties essential for accurate dose calculation. The presented method describes a mathematical framework of how to retrieve the atomic composition of the molecular unit of the damaged material, calculate the linear absorption coefficients for each irradiation load, estimate the areal density of the damaged material, and eventually calculate the dose accurately.

The experimental part gives an example and demonstrates how to apply the developed mathematical approach to calculate the dose for a radiation sensitive material which is subjected to significant damage. Three *ad hoc* models of the radiation damage are compared with the proposed ‘assumption-free’ model. The results show that, if the damage involves mass loss and composition changes (as is the case of PFSA), then it is essential to evaluate the evolution of the material chemistry (elemental atomic array) and material quantity (areal density and/or gravimetrical density) as a function of the exposure time in order to accurately determine the dose. In addition, the knowledge obtained about how the material chemistry evolves with radiation exposure gives a new perspective on mechanisms of radiation damage that will be useful when dealing with radiation-sensitive materials such as PFSA.

7. Related literature

The following references, not cited in the main body of the paper, have been cited in the supporting information: Castner *et al.* (1993); Urquhart & Ade (2002); Ziegler *et al.* (1994).

Acknowledgements

Research supported by a Natural Sciences and Engineering Research Council (NSERC) Discovery grant and the Catalysis Research for Polymer Electrolyte Fuel Cells Network (CaRPE-FC). Measurements were made using the ambient STXM on beamline 10ID1 at the Canadian Light Source (CLS), which is supported by CFI, NSERC, CIHR, NRC and the University of Saskatchewan. We thank Jian Wang and the rest of the SM staff at CLS for their assistance and support of the beamline and STXM.

Funding information

The following funding is acknowledged: Natural Sciences and Engineering Research Council of Canada (grant No. CaRPE-FC).

References

Ade, H. & Hitchcock, A. P. (2008). *Polymer*, **49**, 643–675.

Atkinson, K. (1989). *An Introduction to Numerical Analysis.* Wiley.

Attwood, D. & Sakdinawat, A. (2017). *X-rays and Extreme Ultraviolet Radiation: Principles and Applications.* Cambridge University Press.

Berejnov, V., Rubinstein, B., Melo, L. G. A. & Hitchcock, A. P. (2018). *J. Synchrotron Rad.* **25**, 833–847.

Castner, D. G., Lewis, K. B., Fischer, D. A., Ratner, B. D. & Gland, J. L. (1993). *Langmuir*, **9**, 537–542.

Coffey, T., Urquhart, S. G. & Ade, H. (2002). *J. Electron Spectrosc. Relat. Phenom.* **122**, 65–78.

Egerton, R. F., Konstantinova, T. & Zhu, Y. (2015). *Advances in Imaging and Electron Physics*, edited by M. Berz, P. M. Duxbury and C.-Y. Ruan, Vol. 191, pp. 70–80. Elsevier.

Henke, B. L., Gullikson, E. M. & Davis, J. C. (1993). *At. Data Nucl. Data Tables*, **54**, 181–342.

Hitchcock, A. P. (2012). *Handbook of Nanoscopy*, pp. 745–791. John Wiley & Sons, Ltd.

Hitchcock, A. P., Lee, V., Wu, J., West, M. M., Cooper, G., Berejnov, V., Soboleva, T., Susac, D. & Stumper, J. (2016). *AIP Conf. Proc.* **1696**, 020012.

Hitchcock, A. P., Obst, M., Wang, J., Lu, Y. S. & Tyliszczak, T. (2012). *Environ. Sci. Technol.* **46**, 2821–2829.

Jacobsen, C., Wirick, S., Flynn, G. & Zimba, C. (2000). *J. Microsc.* **197**, 173–184.

Kaznatcheev, K. V., Karunakaran, C., Lanke, U. D., Urquhart, S. G., Obst, M. & Hitchcock, A. P. (2007). *Nucl. Instrum. Methods Phys. Res. A*, **582**, 96–99.

Kilcoyne, A. L. D., Tyliszczak, T., Steele, W. F., Fakra, S., Hitchcock, P., Franck, K., Anderson, E., Harteneck, B., Rightor, E. G., Mitchell, G. E., Hitchcock, A. P., Yang, L., Warwick, T. & Ade, H. (2003). *J. Synchrotron Rad.* **10**, 125–136.

Leontowich, A. F. G., Hitchcock, A. P. & Egerton, R. F. (2016). *J. Electron Spectrosc. Relat. Phenom.* **206**, 58–64.

Leontowich, A. F. G., Hitchcock, A. P., Tyliszczak, T., Weigand, M., Wang, J. & Karunakaran, C. (2012). *J. Synchrotron Rad.* **19**, 976–987.

Leontowich, A. F. G., Tyliszczak, T. & Hitchcock, A. P. (2011). *Proc. SPIE*, **8077**, 80770N.

Ma, Y., Chen, C. T., Meigs, G., Randall, K. & Sette, F. (1991). *Phys. Rev. A*, **44**, 1848–1858.

Martens, I., Melo, L. G. A., Wilkinson, D. P., Bizzotto, D. & Hitchcock, A. P. (2019). *J. Phys. Chem. C*, **123**, 16023–16033.

Mauritz, K. A. & Moore, R. B. (2004). *Chem. Rev.* **104**, 4535–4586.

Melo, L. G. A. (2018). *Soft X-ray spectromicroscopy of radiation damaged perfluorosulfonic acid*, PhD thesis, McMaster University, Canada.

Starodub, D., Rez, P., Hembree, G., Howells, M., Shapiro, D., Chapman, H. N., Fromme, P., Schmidt, K., Weierstall, U., Doak, R. B. & Spence, J. C. H. (2008). *J. Synchrotron Rad.* **15**, 62–73.

Stöhr, J. (1992). *NEXAFS Spectroscopy.* Berlin, Heidelberg: Springer.

Urquhart, S. G. & Ade, H. (2002). *J. Phys. Chem. B*, **106**, 8531–8538.

Wang, J. (2008). *Radiation chemistry by soft X-ray spectromicroscopy.* PhD thesis, McMaster University, Canada.

Wang, J., Botton, G. A., West, M. M. & Hitchcock, A. P. (2009). *J. Phys. Chem. B*, **113**, 1869–1876.

Wang, J., Morin, C., Li, L., Hitchcock, A. P., Scholl, A. & Doran, A. (2009). *J. Electron Spectrosc. Relat. Phenom.* **170**, 25–36.

Wang, J., Stöver, H. D. H., Hitchcock, A. P. & Tyliszczak, T. (2007). *J. Synchrotron Rad.* **14**, 181–190.

WRI (2020). *Mathematica Online*, Wolfram Research Inc., Champaign, IL, USA (https://www.wolfram.com).

Wu, J., Lerotic, M., Collins, S., Leary, R., Saghi, Z., Midgley, P., Berejnov, S., Susac, D., Stumper, J., Singh, G. & Hitchcock, A. P. (2017). *Microsc. Microanal.* **23**, 951–966.

Wu, J., Melo, L. G. A., Zhu, X., West, M. M., Berejnov, V., Susac, D., Stumper, J. & Hitchcock, A. P. (2018). *J. Power Sources*, **381**, 72–83.

Wu, J., Zhu, X., West, M. M., Tyliszczak, T., Shiu, H. W., Shapiro, D., Berejnov, V., Susac, D., Stumper, J. & Hitchcock, A. P. (2018). *J. Phys. Chem. C*, **122**, 11709–11719.

Yan, Z., Hayes, R., Melo, L. G. A., Goward, G. R. & Hitchcock, A. P. (2018). *J. Phys. Chem. C*, **122**, 3233–3244.

Yang, J. & Wang, J. (2017). *Can. J. Chem.* **95**, 1191–1197.

Ziegler, C., Schedel-Niedrig, T., Beamson, G., Clark, D. T., Salaneck, W. R., Sotobayashi, H. & Bradshaw, A. M. (1994). *Langmuir*, **10**, 43994402.